Fast Ion Emission Characteristics of a Forward Laser Plasma Accelerator for Space Propulsion Applications

IEPC-2005-205

Presented at the 29th International Electric Propulsion Conference, Princeton University, October 31 – November 4, 2005

Hideyuki Horisawa* and Masaya Izumi†
Tokai University, Hiratsuka-shi, Kanagawa, 259-1292, Japan

Takehito Takeda‡
Tokai University, Hiratsuka-shi, Kanagawa, 259-1292, Japan

and

Itsuro Kimura§
Professor Emeritus, University of Tokyo, Bunkyo-ku, Tokyo, 113-8856, Japan

Abstract: Fundamental investigations on fast ion emission characteristics from the laser-plasma accelerator employing laser-foil interactions were conducted for an Al-foil target irradiated with an Nd:YAG laser of 1J/pulse with pulse-width of 10nsec. Plasma behaviors were observed through time-gated imaging technique with an ICCD camera. A time-of-flight measurement was also conducted to evaluate ion speeds. In addition, temporal evolutions of electron temperatures and densities were evaluated with electrostatic probes and spectroscopic diagnostics. Moreover, a preliminary one-dimensional particle-in-cell (PIC) simulation was conducted to elucidate acceleration mechanisms. From the results, it was shown that the average and the maximum plasma expansion velocities in a forward direction were about 35 km/s and 160 km/sec, respectively. Also it was shown that the plasma temperature and density were about 2 eV and 10^{10} cm^{-3}.

Nomenclature

c	=	speed of light
$C_m^{(I)}$	=	momentum coupling coefficient observed in the spacecraft frame [I]
E_1	=	input energy to the propellant observed from the spacecraft frame [I]
E_L	=	laser pulse energy
E_{ion}	=	accelerated ion energy
$E_k^{(I)}$	=	kinetic energy of mass element dM observed in the spacecraft frame [I]
dE_1	=	input energy of single laser pulse observed in the spacecraft frame [I]
$E_{total}^{(I)}$	=	total energy of mass element dM observed in the spacecraft frame [I]
$E_0^{(I)}$	=	rest energy of mass element dM observed in the exhaust plasma frame [III]

* Associate Professor, Department of Aeronautics and Astronautics, email: horisawa@tokai.ac.jp.
† Graduate Student, Department of Aeronautics and Astronautics.
‡ Graduate Student, Department of Aeronautics and Astronautics.
§ Professor Emeritus, University of Tokyo.

F_1 = force acting on the spacecraft observed in the spacecraft frame [I]
g_0 = gravitational acceleration measured on Earth [II]
I_L = laser intensity
$I_{sp}^{(I)}$ = specific impulse observed in the spacecraft frame [I]
N_{ion} = number of ions
$\dot{m}_1$ = temporal variation of the spacecraft mass, or propellant mass flow rate, observed from the spacecraft frame [I]
M_1 = mass of the spacecraft observed in the spacecraft frame [I]
dM = mass shot of propellant observed in the exhaust plasma, or propellant, frame [III]
= dM_3
P_1 = input power to the propellant observed from the spacecraft frame [I]
P_L = laser peak power:,
$\check{Q}^{(I)}$ = specific energy-input to the propellant, or energy input for unit mass of plasma exhaust, observed in the spacecraft frame [I]
t_1 = time observed in the spacecraft frame [I]
u_{ion} = speed of ions
v_1 = exhaust speed of the plasma observed from the spacecraft frame [I]
γ_1 = relativistic factor, or Lorentz factor, measured from the spacecraft frame [I]
= $\dfrac{1}{\sqrt{1-v_1^2/c^2}}$
λ_L = wavelength of the laser pulse
$\eta_k^{(I)}$ = energy conversion efficiency observed in the spacecraft frame [I]
τ_L = laser pulse width

Subscripts
1 or (*I*) = quantities observed from the spacecraft frame [I]
2 or (*II*) = quantities observed from the Earth frame [II]
3 or (*III*) = quantities observed from the exhaust plasma frame [III]

I. Introduction

The interaction of ultraintense laser pulses with solid targets leads to generation of fast particles, from x- and γ-ray photons to high energy ions, electrons, and positrons.[1–9] In particular, an interest has developed in ion acceleration by compact high-intensity femtosecond lasers with potential applications for the initiation of nuclear reactions on a tabletop. Experiments now being carried out involve high energy ions generated in the interaction of laser pulses with solid targets as shown in Fig.1. In this case, strong electrostatic fields can be generated through charge separation. The efficiency of the laser energy conversion into a high energy electron component dominates this phenomena. Thermal expansion of the laser-driven plasma and ponderomotive electron expulsion constitute the most well-known examples of the electrostatic-fields production (Fig.1).[9]

For propulsion applications, a collimated plasma beam will be preferable. The collimation requires a planer charge separation, which can be achieved by focusing an intense laser pulse onto the surface of a planar solid-density film. In this case the laser light terminates at the target surface and drives high-energy electrons generated in front of it deep inside the target. Because of the planar charge separation these electrons produce a strong electrostatic field accelerating ions in a forward direction. In this case, high energy electrons expand faster and the ions form a well collimated beam confined in the transverse

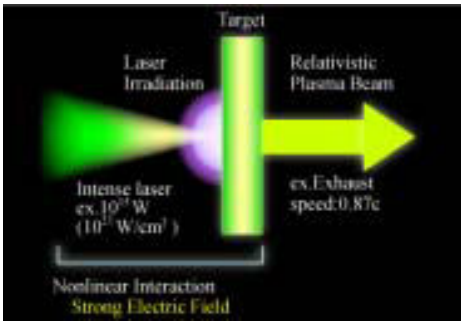

Figure 1. Schematic image of forward laser plasma acceleration through laser-target interaction.

Table 1. Plasma accelerators by an intense laser pulse (λ_L : wavelength of the laser pulse, E_L: pulse energy, τ_L : pulse width, P_L: peak power, I_L: laser intensity, E_{ion}: accelerated ion energy, N_{ion}: number of ions, u_{ion}: velocity of ions, c: speed of the light, I_{sp}: specific impulse).

Laboratory	λ_L [μm]	E_L [J]	τ_L [psec]	P_L [W]	I_L [W/cm^2]	Ions (Target)	E_{ion} [MeV]	N_{ion} /pulse	E_{ion}/E_L	$(u_{ion}/c)^c$	I_{sp} [c] [Msec]
RAL [1]	1.053	30	1.8 ~ 4	–	2 x 10^{18}	Proton (Mylar disk)	4.2 (1.3)[b]	–	0.1	0.094	2.899
RAL [3]	1.053	30	~ 1	–	10^{19}	Proton (CH disk)	12 (1 ~)	–	–	0.158	4.910
RAL [6]	1.053	50	0.9 ~ 1.2	–	5 x 10^{19}	Proton (Al foil)	18 (2 ~)	10^{12}	(0.06)[b]	0.193	6.022
LLNL [4]	1.053	< 1k	0.45	~ 10^{15}	6 x 10^{20}	Proton (Metal foil)	50	–	–	0.317	10.12
LLNL [7]	1.000	–	0.5, 5	~ 10^{15}	3 x 10^{20}	Proton (Plastic CH)	55 (10 ~)	3 x 10^{13}	0.06	0.327	10.63
LLNL [8]	1.000	–	0.5	~ 10^{15}	3 x 10^{20}	Proton (CH polymer)	58 (10 ~)	2 x 10^{13}	0.12	0.336	10.92
LLNL [2 a]	0.400	–	0.01 ~ 0.2	~ 10^{15}	10^{18} ~ 10^{22}	Proton (Al, CH foil)	29	3 x 10^{13}	0.2	0.243	7.667
Osaka U.[5 a]	1.000	–	0.018	~ 10^{15}	1.6 x 10^{22}	Proton (Plasma slab)	~ 1000	–	–	0.875	55.29

[a] results from PIC simulation, [b] average value, [c] estimated value[10,11]

direction by the pinching in the self-generated magnetic field.[5] The ions in the beam expand in the longitudinal direction because the electric charge is not compensated inside. It has been shown that the mechanism of this anisotropic Coulomb explosion is at work in the case of the interaction of a petawatt laser with a thin slab of overdense plasma and accelerates ions up to relativistic energies. The electromagnetic filamentation instability leads to magnetic pinching in the transverse direction and to collimated beam formation.

Recent experimental and theoretical results of laser plasma accelerators in various laboratories are listed in Table 1, in which estimated values of u_{ion}/c, i.e., fraction of the ion velocity to the speed of light, and specific impulse I_{sp}, based on the special theory of relativity, are also added.[10,11] Maximum ion energy of order tens of MeV through the acceleration has been reported in recent studies.[1–8] From the table, as for a proton beam accelerated up to 58 MeV,[8] its speed corresponds to 33 % of the speed of light and the specific impulse Isp of order 10^7 sec. Moreover, in theoretical studies, it was predicted that the relativistic ion beam, u_{ion}/c ~ 87 % and specific impulse I_{sp} ~ 0.55 x 10^8 sec, is achievable with current laser facilities.[5]

Although those accelerators were originally developed for the use of igniters for nuclear fusion reactions, we propose the use for space propulsion applications.[10–12] For the propulsion applications based on the relativistic beams, extremely high values of the specific impulse can be expected through the relativistic effects.[10,11] In cases of operations of this type of thrusters on earth and/or solar orbit, in which solar power is available, the merit of high specific impulse will bring on a significant advantage. The use of this type of propulsion system may also bring some solutions to the problem of the inherent penalty of extremely large mass of propellant required in interstellar flight missions.[10–13]

Since no special nozzle or channel but only a thin film target is needed for the collimated plasma beam formation as shown in Fig.1, the propulsion system employing this technique can be significantly simple and small. In this study, a preliminary investigation is conducted on characteristics of plasmas induced in the forward laser plasma acceleration with a nanosecond laser.

II. Relations of Relativistic High-Specific-Impulse Thrusters

Considering a bunch of exhaust plasma reaching a relativistic speed v_1 (= constant), inducing a thrust F_1, or a momentum change $d(M_1v_1)$, with a mass flow $\dot{m}_1$ or a mass shot dM which is a rest mass element measured at the spacecraft as illustrated in Fig.2, the specific impulse $I_{sp}^{(I)}$ observed onboard, or in the spacecraft frame [I], is expressed as, [14,15]

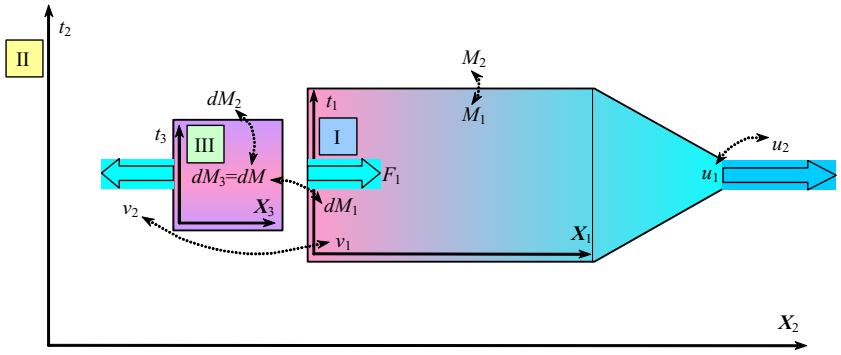

Figure 2. A schematic image of relativistic consideration of thrust performance, or motion of an exhaust plasma, observed from the spacecraft frame [I], the Earth frame [II] and the exhaust plasma frame [III].

$$I_{sp}^{(I)} = \frac{F_1}{\dot{m}_1 g_0} = \frac{\dfrac{d}{dt_1}(M_1 v_1)}{\dfrac{dM}{dt_1} g_0} = \frac{\dfrac{dM_1}{dt_1} v_1}{\dfrac{1}{\gamma_1}\dfrac{dM_1}{dt_1} g_0} = \gamma_1 \frac{v_1}{g_0}. \tag{1}$$

where, the relativistic factor, or Lorentz factor,

$$\gamma_1 = \frac{1}{\sqrt{1 - v_1^2 / c^2}}. \tag{2}$$

The momentum coupling coefficient $C_m^{(I)}$ observed in the spacecraft frame [I], is written as,

$$C_m^{(I)} = \frac{\dfrac{d}{dt_1}(M_1 v_1)}{\dfrac{dE_1}{dt_1}} = \frac{F_1}{P_1} = \frac{\dfrac{d(M_1 v_1)}{dt_1} v_1}{\dfrac{dE_1}{dt_1}} = \frac{v_1 dM_1}{dE_1} = \gamma_1 v_1 \frac{dM}{dE_1}. \tag{3}$$

where, dE_1 is an input energy of the single laser pulse, or an input power P_1, observed in the spacecraft frame [I]. The specific energy-input to the exhaust plasma, or energy input for unit mass of the exhaust plasma, $Q^{*(I)}$ observed in the spacecraft frame [I], is defined as,

$$Q^{*(I)} = \frac{dE_1}{dM}. \tag{4}$$

Then, these product can be expressed as,

$$C_m^{(I)} Q^{*(I)} = \gamma_1 v_1 \frac{dM}{dE_1}\frac{dE_1}{dM} = \gamma_1 v_1 = g_0 I_{sp}^{(I)}. \tag{5}$$

The energy conversion efficiency $\eta_k^{(I)}$ defined as a ratio of kinetic energy ($E_k^{(I)}$) of mass element (dM) of the exhaust plasma to the input energy of single laser pulse (dE_1), observed in the spacecraft frame [I], is expressed as,

$$\eta_k^{(I)} = \frac{E_k^{(I)}}{dE_1}. \tag{6}$$

Here, the relativistic kinetic energy ($E_k^{(I)}$) of mass element (dM) of exhaust plasma observed in the spacecraft frame [I], is expressed as,

$$E_k^{(I)} = E_{total}^{(I)} - E_0^{(I)} = dM_1 \cdot c^2 - dM \cdot c^2 = (\gamma_1 - 1) dM \cdot c^2. \tag{7}$$

Here, $E_{\text{total}}^{(I)}$ is the total energy of mass element dM observed in the spacecraft frame [I], and $E_0^{(I)}$ is the rest energy of mass element dM observed in the exhaust plasma frame [III]. Then, the energy conversion efficiency is written as,

$$\eta_k^{(I)} = \frac{(\gamma_1 - 1)c^2 dM}{dE_1} = C_m^{(I)} I_{sp}^{(I)} \frac{g_0(\gamma_1 - 1)}{\gamma_1} \frac{c^2}{v_1^2} \tag{8}$$
$$= \frac{g_0}{\gamma_1 + 1} C_m^{(I)} I_{sp}^{(I)} = \frac{\gamma_1}{\gamma_1 + 1} C_m^{(I)} v_1.$$

The efficiency cannot exceed unity, or $\eta_k^{(I)} \le 1$, then,

$$C_m^{(I)} I_{sp}^{(I)} \le \frac{\gamma_1 + 1}{g_0} \tag{9}$$
$$\le \frac{\gamma_1}{g_0} \quad (\text{when } \gamma_1 >> 1),$$

or,

$$C_m^{(I)} \le \frac{\gamma_1 + 1}{\gamma_1 v_1} \tag{10}$$
$$\le \frac{1}{v_1} \quad (\text{when } \gamma_1 >> 1).$$

Then,

$$dE_1 \ge \frac{\gamma_1^2}{\gamma_1 + 1} v_1^2 dM \tag{11}$$
$$\ge \gamma_1 v_1^2 dM \quad (\text{when } \gamma_1 >> 1),$$

or,

$$P_1 \ge \frac{\gamma_1^2}{\gamma_1 + 1} v_1^2 \dot{m}_1 \tag{12}$$
$$\ge \gamma_1 v_1^2 \dot{m}_1 \quad (\text{when } \gamma_1 >> 1).$$

When, v_1 approaches the speed of light c, or, in a case of the photon rocket, for example,

$$v_1 \to c,\ \gamma_1 \to \infty,\ \frac{\gamma_1}{\gamma_1 + 1} \to 1,\ I_{sp}^{(I)} \to \infty. \tag{13}$$

Then,

$$\eta_k^{(I)} = \frac{g_0}{\gamma_1 + 1} C_m^{(I)} I_{sp}^{(I)} \tag{14}$$
$$\to \frac{g_0}{\gamma_1} C_m^{(I)} I_{sp}^{(I)} = C_m^{(I)} c \le 1.$$

From these relations,

$$C_m^{(I)} \le \frac{1}{c}, \tag{15}$$

$$Q^{*(I)} \ge \gamma_1 c^2, \tag{16}$$

$$dE_1 \ge \gamma_1 c^2 dM, \tag{17}$$

or

$$P_1 \ge \gamma_1 c^2 \dot{m}_1. \tag{18}$$

III. PIC (Particle-In-Cell) Simulation for Investigation of Acceleration Mechanisms

A preliminary PIC (particle-in-cell) simulation was conducted to investigate acceleration mechanisms of laser-film interaction.[16] A schematic of the simulation model is shown in Fig.1. As shown in this figure, assuming a planar electromagnetic wave, having vertical electric field component E_y and horizontal magnetic field component B_z, as a laser beam which impinges to a thin solid film and penetrates into it, a 1-dimensional (or 1.5-D) simulation considering particle motion in x-direction was conducted.

A. Temporal Behaviors of Particles and Electromagnetic Wave

Temporal evolutions of vertical electric field of an incident laser pulse and x-component velocity of the particles, which are electrons in these cases, at an initial phase of 0.5 to 2.5 fsec after laser irradiation for the laser intensity I_L = 2.7 x 10^{17} W/cm^2, wavelength λ_L = 100 nm, target thickness t = 400 nm are shown in Fig.***. In this figure, positions of top and bottom surfaces of the target are indicated as dotted lines. At 0.5 fsec at which only one wavelength of the laser beam is penetrating into the target, electric field strength is slightly reduced inside the target. At the same time, particles inside the target at one wavelength depth are accelerated gaining axial velocity, or x-component velocity of about 8 % of the speed of light at maximum ((d) and (e)). After 1.5 fsec at which the laser wave is emitted from a bottom surface of the target, its field strength is decreased down to about 50 % ((b) and (c)). Then bunch of the particles start jumping out from the bottom surface, or being accelerated into the vacuum ((e) and (f)). As can be seen in (f), the maximum velocity of the accelerated particles is about 11 % of the speed of light in this case.

Temporal evolutions of vertical electric field and axial velocity of the particles at an initial phase for the higher laser intensity I_L = 6.8 x 10^{17} W/cm^2, wavelength λ_L = 100 nm, target thickness t = 400 nm are shown in Fig.***. Although temporal behaviors of the electric field and particles are similar to the lower intensity case, particles inside the target at one wavelength depth at 0.5 fsec are gaining axial velocity of about 10 % of the speed of light at maximum ((d) and (e)). After 1.5 fsec at which the laser wave is emitted from a bottom surface of the target, its field strength is decreased down to about 30 % ((b) and (c)). Then bunch of the particles are accelerated into the vacuum ((e) and (f)). As can be seen in (f), the maximum velocity of the accelerated particles is about 18 % of the speed of light in this case.

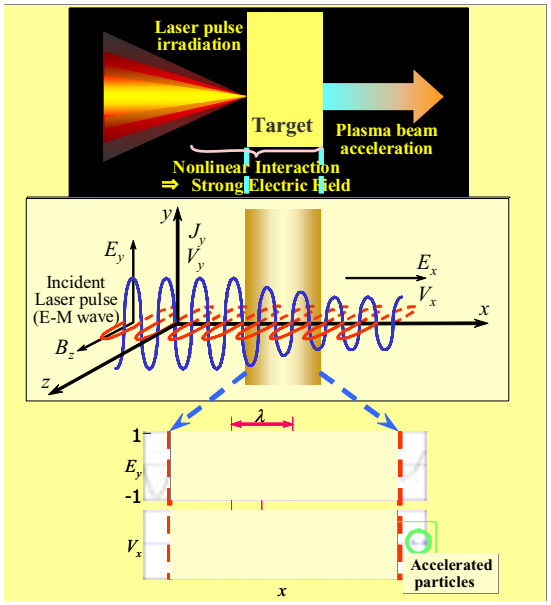

Figure 3. 1-D PIC simulation model.

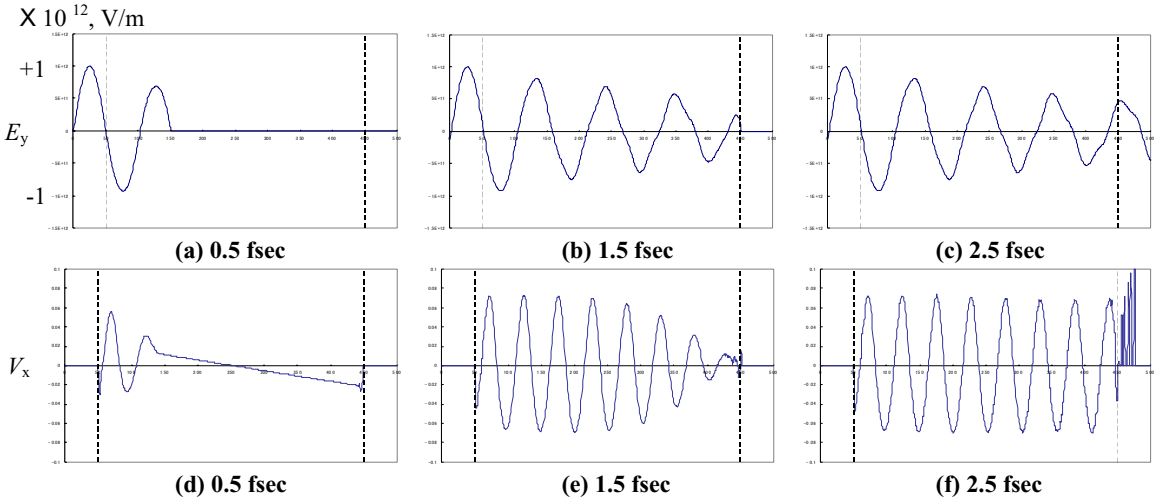

Figure 4. Temporal evolution of vertical electric field E_y and axial velocity V_x for laser intensity $I_L = 2.7 \times 10^{17}$ W/cm^2, wavelength $\lambda_L = 100$ nm, target thickness $t = 400$ nm.

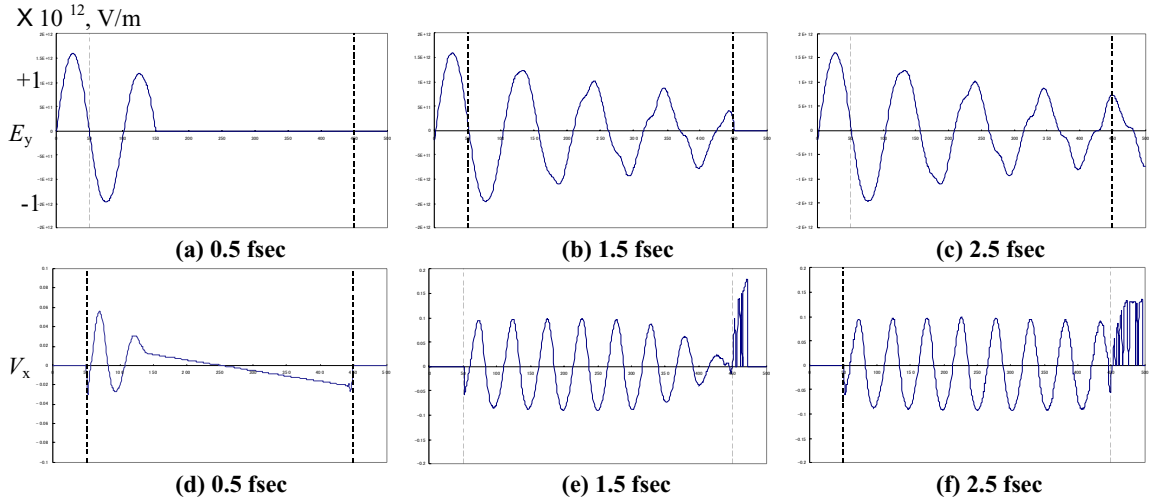

Figure 5. Temporal evolution of vertical electric field E_y and axial velocity V_x for laser intensity $I_L = 6.8 \times 10^{17}$ W/cm^2 , wavelength $\lambda_L = 100$ nm, target thickness $t = 400$ nm.

B. Acceleration Mechanism

In (e) and (f) of Figs.4 and 5, particle motion in axial direction inside the target is occurring at positions where electric field gradients taking maximum values. Inside the target, the particles are having oscillating velocities for forward and backward directions with their wavelength of a half of the incident laser wave. Also it can be seen that these particle motions or waves are in phase with the incident laser beam. At the bottom surface and outside the target, particles are being accelerated only in the forward direction having higher velocities than those of inside the target. From these results, it was confirmed that particles are being accelerated in phase, or on the wave, with the incident laser beam.

In (b) and (c) of Figs.4 and 5, it can be seen that some parts of the electric wave inside the target are decreased in their wave heights and distorted in their wave shapes having nonlinear components. From the spectral analysis, it was confirmed that most of the components was the third harmonic wave of the incident wavelength of the laser beam. Through this process including the nonlinear phenomena, particles are given the kinetic energy or accelerated into vacuum.

Mechanisms contributing the particle acceleration are as follows; at first, the particles are accelerated to vertical- or y-direction inducing velocity in y-direction V_y by the vertical electric field E_y of the incident laser beam. At the same time, with interaction of the vertical velocity V_y and horizontal magnetic field B_z of the laser beam, or Lorentz force $F_x = qV_yB_z$, the particles are accelerated to x-direction.

IV. Fundamental Experiments with GW-Pulse Lasers

Although conventional experiments listed in Table 1 have been using ultra-high-power lasers, or T (tera)-watt / P (peta)-watt, lasers for investigations of fundamentals in high-energy nuclear physics, our present study is using a G (giga)-watt laser system for system simplicity.

A. ICCD Camera and Spectroscopic Observation of Laser-Induced Plasma

In order to observe temporal behaviors, or velocity and temperature, of laser-induced plasma, ICCD camera observation and spectroscopic diagnostics were conducted. A schematic of an experimental setup is shown in Fig.6. As for a laser oscillator, a Q-switched Nd:YAG laser (BMI, 5022DNS10, wavelength: 1064 nm, maximum pulse energy: 1.4 J, pulse width: 5 nsec (FWHM)) was utilized. Focusing a laser pulse on a thin foil target with a focusing lens (f = 100 mm) in vacuum (4.0×10^{-4} Pa), the laser-induced plasma was generated. In this experiment, an aluminum foil of 12μm thick mounted on a y-z stage was employed as the target.

Plasma behaviors were observed with an ICCD camera (Oriel Instruments, INSTASPECTMV, minimum gate width: 2 nsec) and a spectrum multi-channel analyzer (Oriel Instruments, MS257). Generating an arbitrary delay with a delay generator triggered by a Q-switch output signal, the ICCD camera was synchronized with a laser pulse. Since this phenomenon was highly reproducible, it was possible to obtain images of temporal behaviors of a plasma formation process with 2nsec resolution through changing the delay timing. Images from the ICCD camera were processed into colored contour lines proportional to the emission intensity distribution with image processing software (MEDIA CYBERNETICS, Image-Pro-Plus).

For the spectroscopic measurement, emission from the plasma was focused on an edge of an optical fiber and then introduced through it to the spectrum multi-channel analyzer. Plasma spectra of the range of 260 to 600 nm were captured with a spectral resolution of 0.08 nm and a temporal resolution of 2 nsec. From the temporal changes of the spectra and NIST Spectra Line Database,[17] temporal evolution of electronic excitation temperature of the plasma was estimated with the line pair method.

B. Temporal Evolution of Ion Currents and Plasma Characteristics

Temporal evolutions of ion current were also observed with a Faraday cup. The Faraday cup with stainless grids of 400 mesh/inch and 10 mm in diameter was placed at 100 mm and 150 mm away from the target surface on the center line of the plume. The ion currents were monitored by an oscilloscope (LeCroy, 9374TM, range: 1 nsec/div ~ 5 msec/div). Estimating the time-of-flight of ions between two positions, a speed of ions was calculated.

Temporal evolutions of plasma temperatures and densities were also measured by electrostatic probe diagnostics of the plasma plumes. An electrostatic single-probe consisting of a tungsten rod of 0.1 mm in diameter

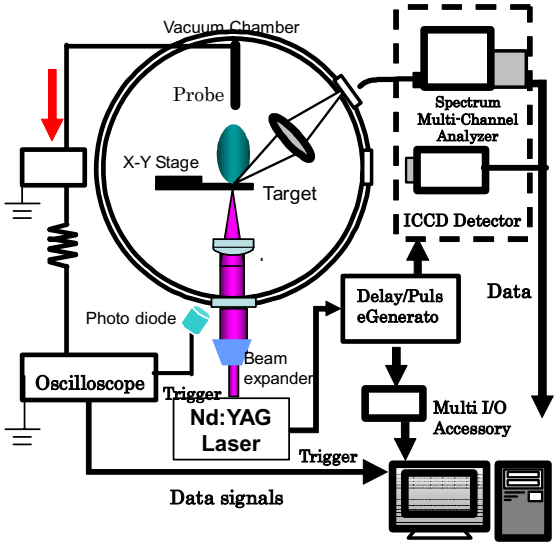

Figure 6. Schematics of experimental setup.

and 1.8 mm in length was placed at 100 mm away from the target on the centerline. In general the single probe measurement is applied to relatively stable, or steady state, plasma with its characteristic time scale of at least 1 msec. On the other hand, as the time scale of the laser-ablation plasmas induced by pulsed lasers is about nanoseconds to microseconds, a high-resolution measurement in time scales is required. Since these phenomena are highly reproducible, it was possible to obtain temporal changes of probe currents with an oscilloscope (Tektronix, spectral width 300 MHz, maximum sampling rate 2.5GS/sec) for various probe bias cases for identical event. Replotting a probe current-voltage characteristic for each time, or taking a temporal slice of a current-voltage characteristic for each time, temporal evolutions of plasma temperature and density were estimated.[18]

V. Experimental Results and Discussion

A. ICCD Camera Observation of Laser-Induced Plasma

Temporal evolution of ICCD camera images of laser-induced plasmas for laser energy of 1 J/pulse is shown in Fig.7. As shown in these figures, rapid plasma injection is occurring on both front and rear surfaces, or both backward and forward accelerations are observed. Also, it can be seen that plasma emissions occurring in the forward direction are more intense than those of backward direction at initial 100 nsec. Although the backward plasma is expanding radially in a diffuse manner, the forward plasma in an initial phase is more directed and collimated in an axial direction. However, after 130 nsec, the forward plasma starts expanding radially with similar speed as a radial component of the backward plasma. This is probably occurring after the formation of a through-hole on a focal point of the target surface. Through the hole, some part of the backward plasma induced on a front surface penetrates and then scatters into radial directions behind a rear surface.

In order to estimate velocities of the plasmas, temporal variations of axial positions of the plasma wave front expanding from the target surface are estimated. Here, the wave front is defined as a plasma-plume emission-contour having identical intensity. Results of these estimated values for higher laser energy case (1 J) are plotted in Fig.8. In this figure, positions having various emission intensities from each image are plotted. Each intensity value is defined as a ratio of a local emission intensity to a maximum intensity in whole area of each image. It can be seen that positions of each intensity value are increasing linearly, or moving at constant speeds. From the results of Fig.8, a velocity distribution is plotted in Fig.9. In this figure, lower velocities of less than 30 km/sec are not plotted. It can be seen that the plasma injected in a forward direction has a maximum speed of about 160 km/sec. Since the intensities take a maximum value at about 35 km/sec, an average speed, or most probable speed, can be about 35 km/sec.

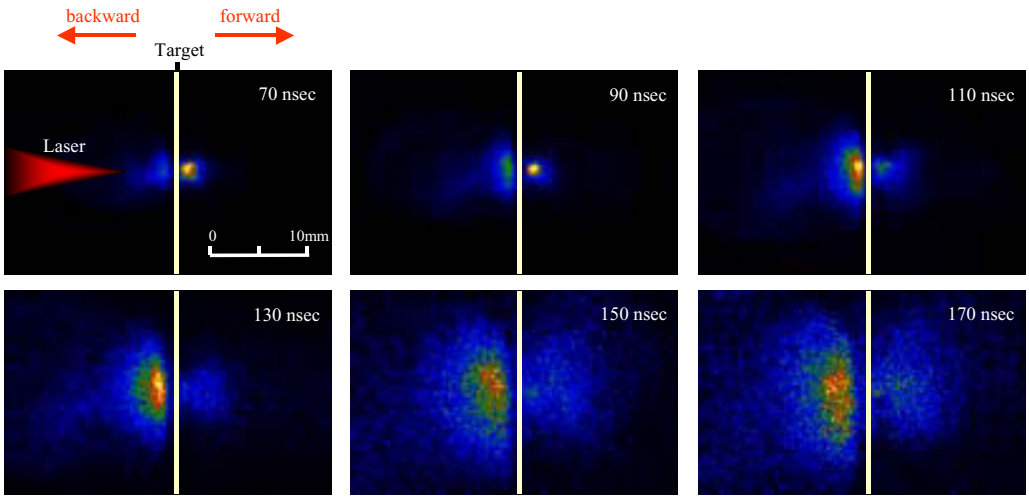

Figure 7. ICCD camera images of laser-induced plasmas accelerated in forward / backward direction (Nd:YAG, pulse energy: 1 J, pulse width: 10 nsec, ICCD gate width: 10 nsec, 20 nsec / frame).

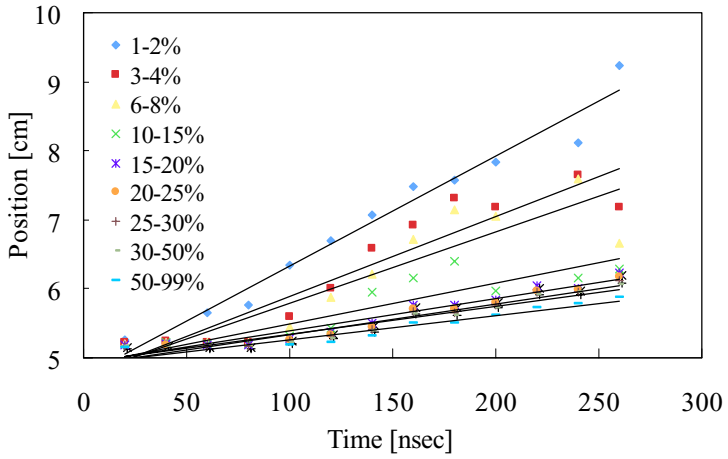

Figure 8. Expanding rates of a forward plasma, plotting positions of each emission intensity value from each 10 nsec-image, which is defined as a ratio of emission intensity to a maximum intensity in whole area of each image (Nd:YAG, pulse energy: 1 J).

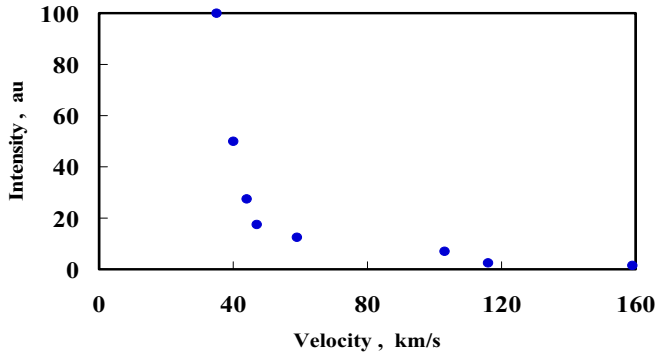

Figure 9. Velocity distribution estimated from Fig.8.

B. Spectroscopic Diagnostics of Laser-Induced Plasma

Temporal evolutions of spontaneous emission spectra of a laser-induced forward plasma taken with the gate width of 10 nsec are shown in Fig.10. Since a spectral range in a single scan was about 200 nm in these cases, results from two scans with different center wavelengths were combined at dotted line resulting in a discontinuity at 400 nm in each figure. At 20 nsec, continuous components of spectra can be seen having significantly stronger intensities than any atomic and ionic line spectra, and it is difficult to identify these line spectra. These continuous components are probably due to the inverse-bremsstrahlung radiation of electrons and/or the blackbody radiations from atoms and ions.

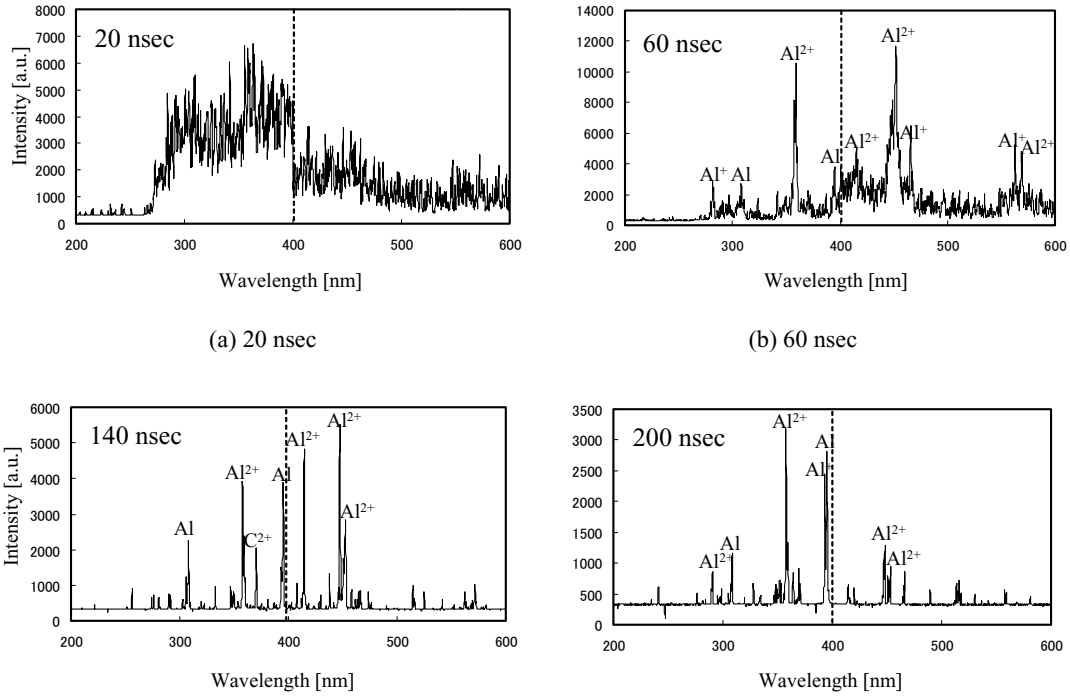

Figure 10. Spectra of a forward plasma after laser pulse irradiation.

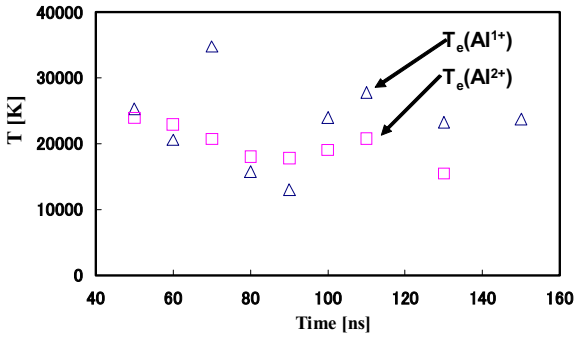

Figure 11. Temporal evolutions of electronic excitation temperatures of aluminum ions estimated with the two line method from spontaneous emission spectra of a laser-induced forward plasma.

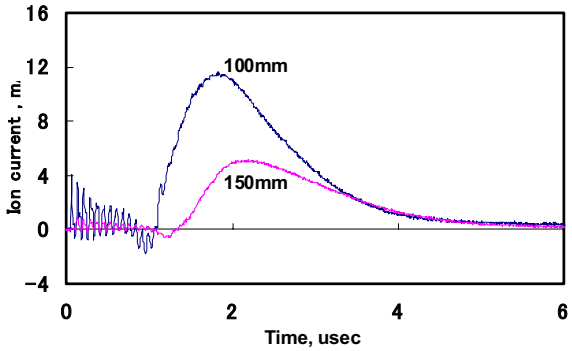

Figure 12.Temporal evolutions of ion currents observed at different positions.

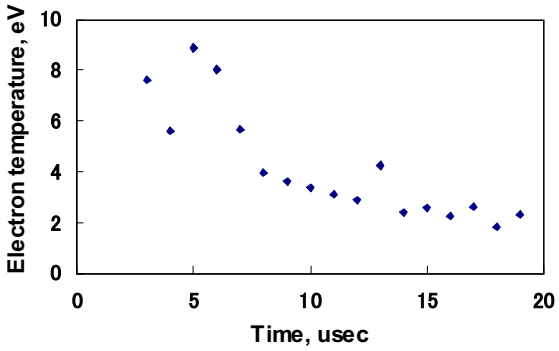

Figure 15. Temporal evolution of electron temperature.

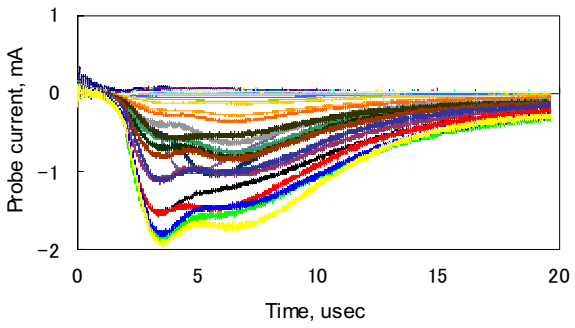

Figure 13. Temporal evolutions of probe currents for different probe bias cases.

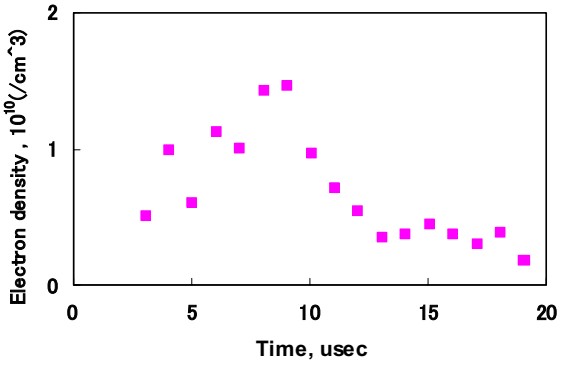

Figure 16. Temporal evolution of electron density.

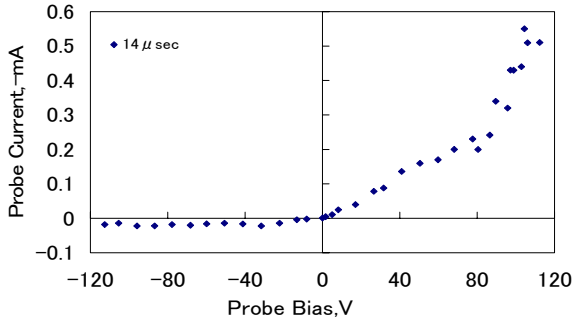

Figure 14. Typical plots of probe current and voltage characteristic replotted from a temporal slice of data of Fig.13 at 14 μsec.

After 60 nsec, numbers of observable line spectra of aluminum ions start increasing and the continuous components being reduced. It is presumed that around this time ions are being formed and accelerated into the observation region. In these figures, observable spectra are of aluminum atoms, and its ions including singly-, doubly- and triply ionized species. Ionic carbons and oxygens are also observed, which are probably the absorbed species in the target surface while having been exposed in atmosphere before placed in vacuum.

Electronic excitation temperatures of singly- and doubly- ionized aluminum ions are estimated with the two line method from the spontaneous emission spectra of those ions at each time. Temporal evolutions of those temperatures are shown in Fig.11. Although some scatters of the data can be seen, the temperatures are about 20,000 K and slightly decreasing with time.

C. Ion Speed Estimation with Time-Of-Flight Measurement

Temporal evolutions of ion currents taken at 100 mm and 150 mm away from the target surface are shown in Fig.12. It can be seen that current peaks are observed at 1.82 μsec and 2.19 μsec for 100 mm and 150 mm cases, respectively. An average ion speed was estimated from the spatial gap between two points (50 mm) divided by the time difference of 0.37 μsec between the peaks, namely as 135 km/sec. This value of the plasma exhaust speed is consistent with the result of ICCD measurement of Fig.9 at 5 % emission intensity.

D. Single Electrostatic Probe Diagnostics of Laser-Induced Plasma

Temporal evolutions of probe currents for various probe bias cases are shown in Fig.13. Taking a temporal slice of a probe current-voltage characteristic for each time for each time, temporal evolutions of plasma temperature and density could be estimated. Figure 14 shows a typical plot of the probe current and voltage characteristic sliced at 14 μsec. As shown in this figure, the typical current-voltage characteristic curve can be obtained through the electrostatic probe. From the current-voltage characteristic obtained through slicing results of Fig.13 at a targeted moment, electron temperature and density could be estimated through a conventional electrostatic probe theory.

Temporal evolutions of electron temperatures and densities are plotted in Figs.15 and 16, respectively. It can be seen that the electron temperature peaks up to about 8 eV at 5 μsec and decreases down to 2 eV at 15 μsec. This result is consistent with those of electronic excitation temperatures (about 20,000 K) of aluminum ions. Meanwhile the electron density peaks up to about 1.5 x 10^{10}cm^{-3} at 8 μsec and decreases down to 3 x 10^{9}cm^{-3} at 13 μsec.

E. Temporal Evolution of Target Potential

In order to elucidate acceleration mechanisms dominating these phenomena, target potentials were also estimated. Temporal evolutions of target potentials relative to a grand potential are shown in Fig.17. It can be seen that the target potential abruptly rises and takes positive values at an initial microsecond, showing a peak value of 130 V, followed by rapid decreases and negative values up to more than sub-millisecond. Although not shown in this figure, it was observed that lager voltages of either positive or negative values are induced on the target in a higher laser energy case. The initial positive voltages indicate that negative particles or electrons in this case are being emitted from the target surface. Moreover, the subsequent negative voltages are due to positive ion emission from the target surface following foregoing electrons. Estimating emission timing of positive ions leaving from a rear surface of the target from results of Figs.12 and 13, signals of the positive ions coincide with drop times of negative voltages in Fig.17. From these results, the acceleration mechanism in this case is that; 1) electrons are emitted from target surface, and 2) ions, repelled each other and attracted by those foregoing electrons, are subsequently emitted from the target through the Coulomb explosion.

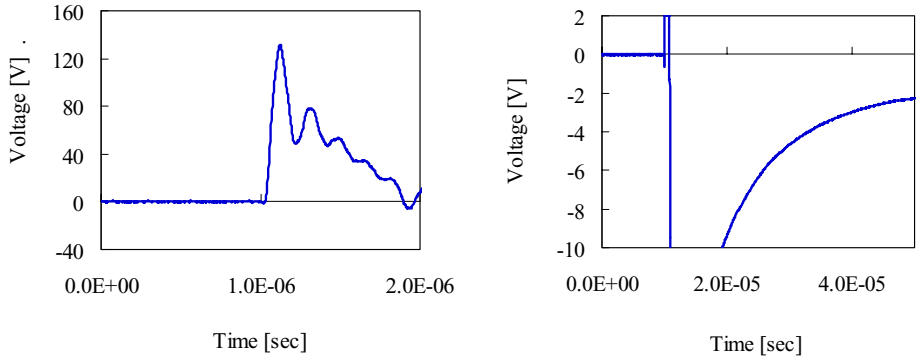

(a) initial microsecond. **(b) subsequent sub-millisecond.**

Figure 17. Temporal evolution of target potential for laser pulse energy of 1 J.

VI. Conclusion

Fundamental investigations on fast ion emission characteristics from the laser-plasma accelerator employing laser-foil interactions were conducted for an Al-foil target irradiated with an Nd:YAG laser of 1J/pulse with pulse-width of 10nsec. Plasma behaviors were observed through time-gated imaging technique with an ICCD camera. A time-of-flight measurement was also conducted to evaluate ion speeds. In addition, temporal evolutions of electron temperatures and densities were evaluated with electrostatic probes and spectroscopic diagnostics. Moreover, a preliminary one-dimensional particle-in-cell (PIC) simulation was conducted to elucidate acceleration mechanisms. From the results, it was shown that the average and the maximum plasma expansion velocities in a forward direction were about 35 km/s and 160 km/sec, respectively. Also it was shown that the plasma temperature and density were about 2 eV and 10^{10} cm^{-3}.

References

[1] Fews, A.P., Norreys, P.A., Beg, F.N., Bell, A.R., Dangor, A.E., Danson, C.N., Lee, P., and Rose, S.J., "Plasma Ion Emission from High Intensity Picosecond Laser Pulse Interactions with Solid Targets," *Physical Review Letters* Vol.73, No.13, 1994, pp.1801-1804.

[2] Lawson, W.S., Rambo, P.W., and Larson, D.J., "One Dimensional Simulations of Ultrashort Intense Laser Pulses on Solid-Density Targets," *Physics of Plasmas*, Vol.4, No.3, 1997, pp.788-795.

[3] Beg, F.N., Bell, A.R., Dangor, A.E., Danson, C.N., Fews, A.P., Glinsky, M.E., Hammel, B.A., Lee, P., Norreys, P.A., and Taterakis, "A Study of Picosecond Laer-Solid Interactions up to 1019 W cm-2," *Physics of Plasmas*, Vol.4, No.2, 1997, pp.447-457.

[4] Roth, M., Cowan, T.E., Hunt, A.W., Johnson, J., Brown, C., Fountain, W., Hatchett, S., Henry, E.A., Key, M.H., Kuehl, T., Parnell, T., Pennington, D.M., Perry, M.D., Sangster, T.C., Christl, M., Singh, M., Snavely, R., Stoyer, M., Takahashi, Y., and Wilks, S.C., "High-Energy Electron, Positron, Ion and Nuclear Spectroscopy in Ultra-Intense Laser-Solid Experiments on the Petawatt," *First International Conference on Inertial Fusion Science and Application*s, 1999.

[5] Sentoku, Y., Liseikina, T.V., Esirkepov, T. Zh., Califano, F., Naumova, N.M., Ueshima, Y., Vshikov, V.A., Kato, Y., Mima, K., Nishihara, K., Pegoraro, F., and Bulanov, S.V., "High Density Collimated Beams of Relativistic Ions Produced by Petawatt Laser Pulses in Plasmas," *Physical Review E*, Vol.62, No.5, 2000, pp.7271 – 7281.

[6] Clark, E.L., Krushelnick, K., Davis, J.R., Zepf, M., Tatarakis, M., Beg, F.N., Machacek, A., Norreys, P.A., Santala, M.I.K., Watts, I., and Dangor, A.E., "Measurements of Energetic Proton Transport through Magnetized Plasma from Intense Laser Interactions with Solids," *Physical Review Letters*, Vol.84, No.4, 2000, pp.670-673.

[7] Hatchett, S.P., Brown, C.G., Cowan, T.E., Henry, E.A., Johnson, J.S., Key, M.H., Koch, J.A., Langdon, A.B., Lasinski, B.F., Lee, R.W., Mackinnon, A.J., Pennington, D.M., Perry, M.D., Phillips, T.W., Roth, M., Stangster, C., Singh, M.S., Snavely, R.A., Stoyer, M.A., Wilks, S.C., and Yasuike, K., "Electron, Photon, and Ion Beams from the Relativistic Interaction of Petawatt Laser Pulses with Solid Targets," *Physics of Plasmas*, Vol.7, No.5, 2000, pp.2076-2082.

[8] Snavely, R.A., Key, M.H., Hatchett, S.P., Cowan, T.E., Roth, M., Phillips, T.W, Stoyer, M.A., Henry, E.A., Sangster, T.C., Singh, M.S., Wilks, S.C., MacKinnon, A., Offenberger, A., Pennington, D.M., Yasuike, K., Langdon, A.B., Lasinski, B.F., Johnson, J., Perry, M.D., and Campbell, E.M., "Intense High-Energy Proton Beams from Petawatt-Laser Irradiation of Solids," *Physical Review Letters*, Vol.85, No.14, 2000, pp.2945-2948.

[9] Maksimchuk, A., Gu, S., Flippo, K., Umstadter, D., and Bychenkov, V., Yu.,"Forward Ion Acceleration in Thin Films Driven by a High-Intensity Laser," *Physical Review Letters*, Vol.84, No.18, 2000, pp.4108-4111.

[10] Horisawa, H., and Kimura, I., "Characterization of Novel Laser Particle Accelerators for Space Propulsion," AIAA 2000-3487 (2000).

[11] Horisawa, H., and Kimura, I., "Laser Plasma Accelerator for Space Propulsion," AIAA 2001-3662 (2001).

[12] Horisawa, H., Kuramoto, H., Oyaizu, K., Uchida, N., and Kimura, I., "Fundamental Study of a Relativistic Laser-Accelerated Plasma Thruster," *Beamed Energy Propulsion: First Intl. Symp. Beamed Energy Propulsion*, 2003, pp.411–422.

[13] Kammash, T. "Advanced Space Propulsion with Ultra-Fast Lasers," *Beamed Energy Propulsion: First Intl. Symp. Beamed Energy Propulsion*, 2003, pp.411–422.

[14] Stuhlinger E., *Ion Propulsion for Space Flight*, McGraw-Hill (1964).

[15] Kimura, I., *Rocket Engineering*, Yokendo (1993) (in Japanese).

[16] Birdsall, C. K., and Langdon, A. B., *Plasma Physics via Computer Simulation*, Adam Hilger (1991).

[17] The NIST spectra Line Database, http://physics.nist.gov/cgi-bin/atData/main_asd.

[18] Weaver, I., Martin, G. W., Graham, W. G., Morrow, T., and Lewis, C. L. S., "The Langmuir Probe as a Diagnostic of the Electron Component within Low Temperature Laser Ablated Plasma Plumes," *Review of Scientific Instruments*, Vol.70, No.3, 1999, pp.1801–1805.